Broadband vibration isolation in a deployable telescopic baffle exploiting post-buckling thrust tube dynamics

Vladimir Yotov
Te Pūnaha Ātea - Space Institute
University of Auckland
Auckland, New Zealand
vladimir.yotov@auckland.ac.nz

Tsvetan Yotov
Te Pūnaha Ātea - Space Institute
University of Auckland
Auckland, New Zealand
t.v.yotov@gmail.com

Mattia Longato
Te Pūnaha Ātea - Space Institute
University of Auckland
Auckland, New Zealand
mattia.longato@auckland.ac.nz

Guglielmo S. Aglietti
Te Pūnaha Ātea - Space Institute
University of Auckland
Auckland, New Zealand
g.aglietti@auckland.ac.nz

Mark Honeth
Te Pūnaha Ātea - Space Institute
University of Auckland
Auckland, New Zealand
mark.honeth@auckland.ac.nz

Christoph Bamann
Vyoma GmbH
München, Germany
christoph.bamann@vyoma.space

***Abstract*—Baffle designs for microsatellite optical instruments are typically constrained by a strict trade-off: motorised telescopic mechanisms provide structural rigidity but incur significant mass and complexity penalties, whereas flexible deployable shrouds cannot provide the deterministic geometry necessary for high-precision optical rejection.**

Recently, a class of passively deployable, rigid telescopic baffles that reconcile launch volume restrictions and in-orbit geometry requirements have been developed. The architecture employs a nested segment arrangement with wire-driven actuation, stabilised via built-in geometrical constraints and pre-tension. The second generation of baffles discussed here features an integrated design, including an opening protective lid and a supporting thrust tube that contains the optical instrument.

When subjected to high lateral loads, the thrust tube exhibits favourable attenuation properties, effectively acting as a geometrically nonlinear acceleration limiter for the telescopic structure during launch. Intermittent operation in a post-buckling regime, with purely elastic amplitude-dependent softening, provides the principal attenuation mechanism. Qualification tests demonstrate significant broadband transmission loss, with no signs of structural or functional degradation detected a posteriori. Initial empirical characterisation of this isolation property clearly shows that the current design inherently maintains a substantially lower vibration environment at the baffle interface compared to typical linearly behaving support structures.

***Index Terms*—Deployable baffle, Thrust tube dynamics, Post-buckling regime, Nonlinear isolator**

I. Introduction

Suppression of stray light is a primary design consideration for high-performance optical payloads such as star trackers and telescopes, since light contamination effectively degrades detection sensitivity and compromises the attainable signal-to-noise ratio (SNR). Consequently, optical baffles represent a necessary component to prevent undesirable off-axis illumination of detectors by direct and reflected sunlight [1]–[5].

From a structural perspective, conventional baffles comprise several fixed, rigid frustums. While they do not sustain significant loads beyond self-support, they dictate the external dimensions of the instrument, so becoming a primary contributor to payload volume [6], [7]. This introduces a direct conflict with the strict spatial limitations imposed by launch vehicle fairings. In effect, deployable baffles that stow during launch and extend in orbit to the required exclusion angle geometry [8], [9] constitute a viable solution [10]–[13].

Nevertheless, existing architectures impose a trade-off. Motorised telescopic mechanisms admit lower geometric tolerances in the deployed state, which is optically favourable, but achieved at the expense of increased mass and complexity. This often renders them unfeasible for microsatellite and rideshare missions, restricted by their small form factor and relatively limited financial budgets. Conversely, flexible shrouds are highly compact but lack a fully deterministic extended shape, impeding their applicability to high-performance spacecraft optics [14]. Circumventing both sets of issues implies the development of passively actuated, kinematically reliable deployable baffles [15], [16].

II. Passive telescopic baffles

A. First generation

Recently, completely passive baffles actuated by preloaded torsion springs and released by a burnwire systems have been devised and successfully used on CubeSats [17], [18]. Subsequent refinements have led to entirely wire-driven deployment mechanisms being proposed [19]. This enhanced concept enables configuration scaling viable to extended lengths in excess of 1 m, whilst practically eliminating end-of-deployment mechanical shock.

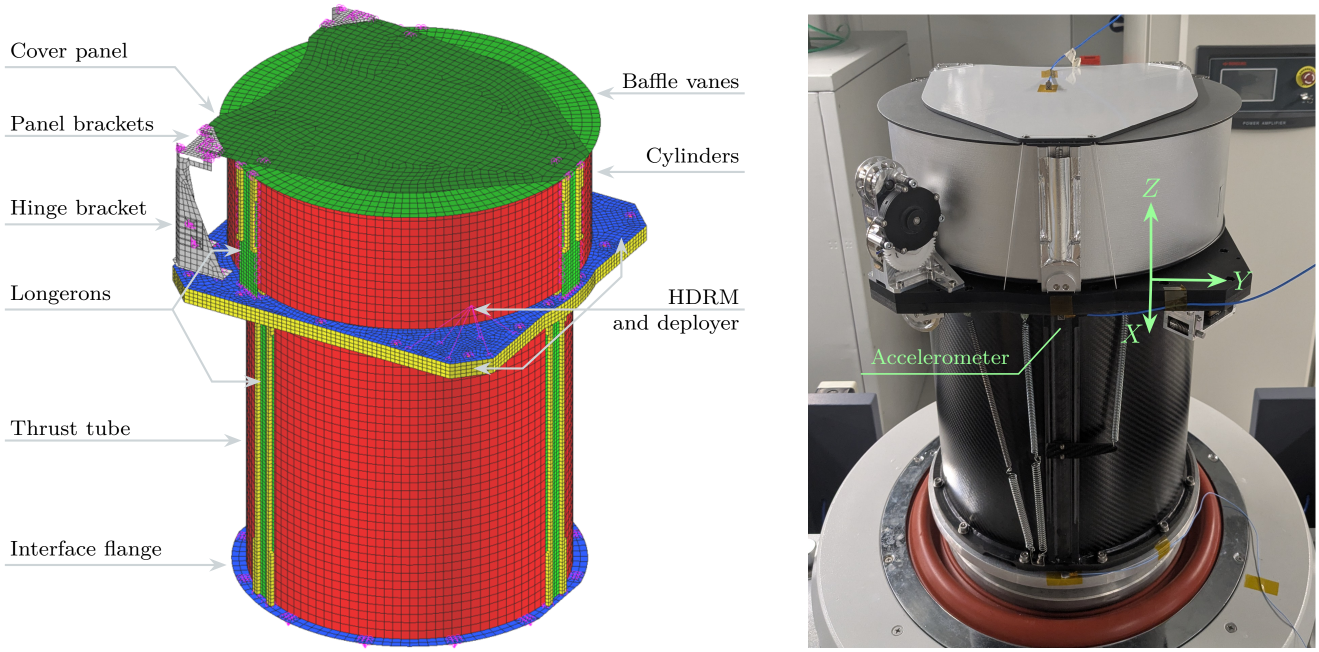

(a) Annotated FE model

(b) Qualification model

Figure 1: Second-generation deployable baffle (stowed)

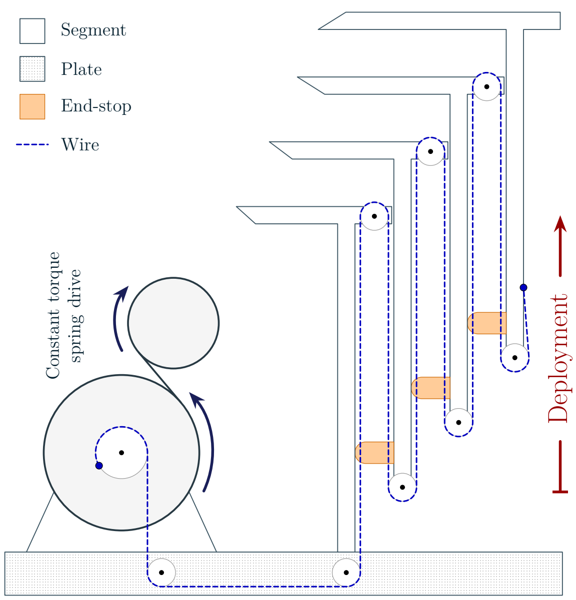

Figure 2: Wire routing schematic for a baffle with sequentially-deployable telescopic segments

The resultant first-generation telescopic baffle consisted of multiple concentric carbon fibre reinforced plastic (CFRP) cylindrical segments driven by a constant torque spring [20]. Motorisation was achieved through a system of tensioned Dyneema wires routed along the structure, moderated by a custom passive eddy-current damper to further restrict deployment velocity and minimise end-of-run shock without introducing significant friction at low speeds. The stowed configuration was locked by a hold-down and release mechanism (HDRM) utilising a redundant burnwire system. Launch survivability and repeatable deployment kinematics of the proposed architecture have been validated via extensive vibration and thermal vacuum chamber (TVAC) test campaigns in adherence to common standards [21], [22].

The particular industrial motivation underpinning this work was support for Vyoma GmbH's forthcoming space situational awareness (SSA) microsatellite constellations, intended to provide space-based orbital debris monitoring and to improve collision avoidance [23]. It fits within the broader context of rapidly expanding low Earth orbit (LEO) operations [24], with tens of thousands of new satellites projected to be launched within a decade [25], [26]. Nonetheless, while incited by LEO sustainability demands, the passive telescopic baffle design is suitable to a wide range of missions.

B. *Second generation*

Building upon expertise from the first generation, a second iteration of the passive deployable baffle has been developed [27]. Its topology is characterised by a fully integrated design, featuring an independent opening protective lid and a supporting CFRP thrust tube enclosing the primary optical instrument. The stowed baffle finite element (FE) model with labelled major components is shown alongside the qualification model (QM) hardware in Figure 1.

The telescopic portion employs four nested concentric segments, each consisting primarily of a vane and thin wall, where the geometry is determined by the optical requirements and

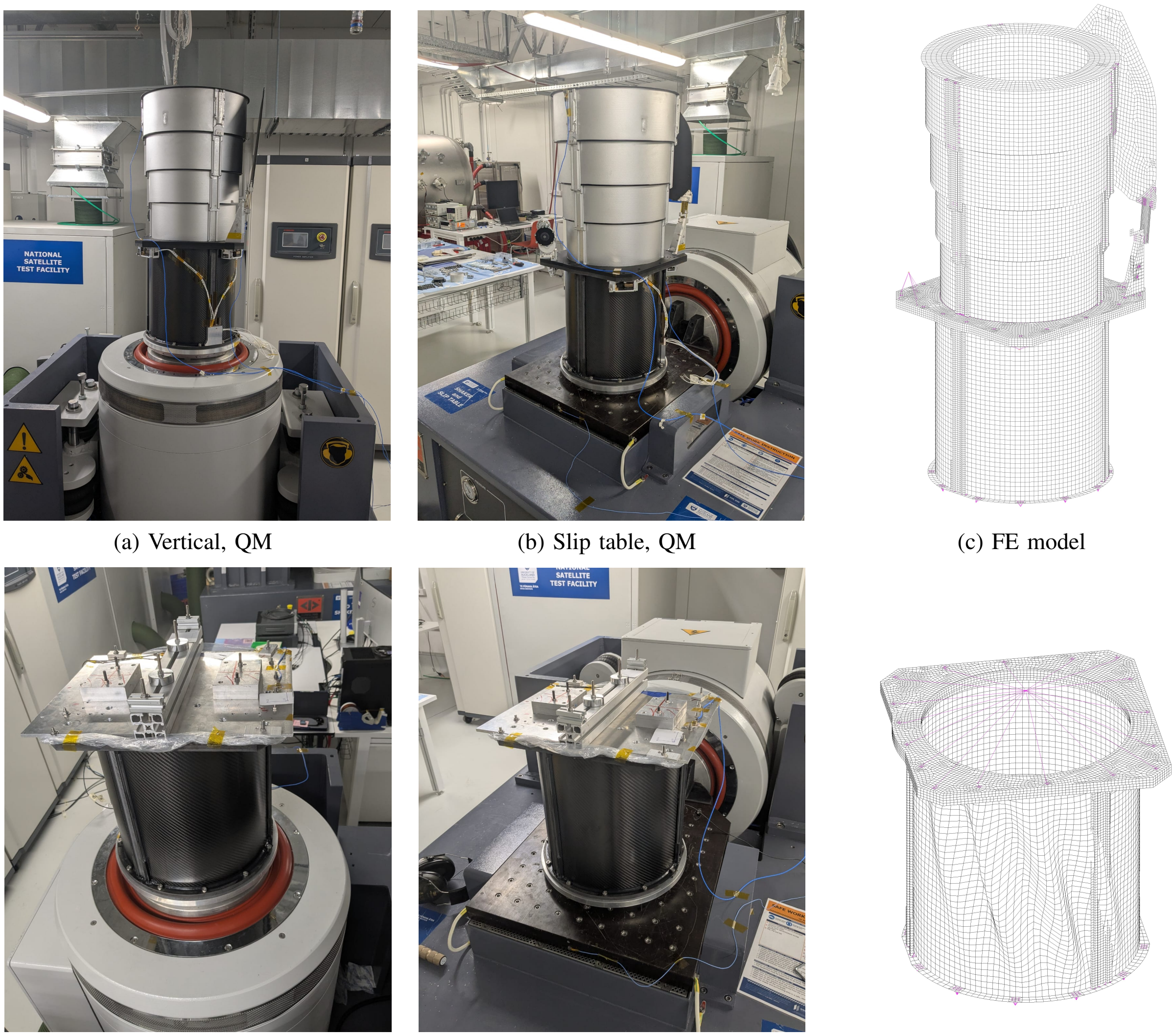

(a) Vertical, QM

(b) Slip table, QM

(c) FE model

(d) Vertical, dummy

(e) Slip table, dummy

(f) FE buckled shape

Figure 3: Preliminary testing and FEA. Dynamics characterisation of the deployed QM in (a)-(c). Vibration testing and buckling analysis of the thrust tube with a stowed telescopic assembly and lid dummy mass in (d)-(f)

volume constraints. Each baffle segment has three rigid longerons spaced 120° apart around the cylindrical segment wall. They incorporate guide rails and flange stops for mechanical restraint and attach to the flat annular vane on one side. The latter also bonds to the cylinder's top edge.

Deployment relies on a passive wire system driven by a constant-torque spring, schematically illustrated in Figure 2. This arrangement yields a sequential extension of the cylinders in an inner-to-outer order. It requires a lower driving force and is more robust to local variations in friction compared to a synchronised deployment. The driving line spatial routing has been devised such that the mechanism inherently self-stabilises solely through its geometry and pre-tension, fully eliminating dependence on active actuators. A CFRP plate housing the HDRM, deployer and Dyneema wire lines interfaces the thrust tube and telescopic subassembly.

Notably, the latter reduces stowed volume by approximately 70% compared to optically equivalent fixed baffles, whilst still satisfying the natural frequency (NF) requirements prescribed by the spacecraft bus provider. Analogously to the first generation, it was ensured by design that all eigenfrequencies in the operational state exceed 10 Hz, such that potential interference with the satellite's attitude determination and control system (ADCS) is mitigated. This is largely dictated by the mass properties of the lid and equivalent stiffness of the dual tape spring-based bistable hinges it is attached on. The latter were stringently optimised to supply sufficient preload in the closed state, necessary for deployment upon burnwire activation, alongside adequate rigidity in the deployed state and a minimal terminating mechanical shock.

Overall, the revised architecture delivers a drastically simplified manufacturing process and integration, reduced HDRM arming complexity and a total mass of under 5 kg, compared to 6.1 kg for the first-generation baffle. Simultaneously, improved thermal coating selection for the exterior surface is anticipated to enhance both optical performance and environmental durability on-orbit.

In the remainder of this article, Section III discusses finite element analysis (FEA) and vibration tests for baffle dynamics characterisation, as well as the formal qualification and acceptance campaigns. Section IV elaborates on exploiting elastic amplitude-dependent softening of the thrust tube for broadband attenuation under high-level lateral loads. Conclusions are given in Section V.

III. Analysis and testing

A. FE modelling

Detailed FE models of the baffle, both stowed and extended, were constructed. Meshing was done in MSC Patran using predominantly quadrilateral shell elements. Fasteners were modelled as 6-degree of freedom (DOF) equivalent springs connecting rigid multipoint constraints. Boundary conditions for the contacts between the telescopic baffle longerons and the plate were approximated in accordance with FEA and experimental validation from the first generation, cf. [20]. Expected material properties, particularly for the CFRP comprising the majority of the structural mass, were also incorporated in the model from previous characterisation tests. MSC Nastran was the solver used throughout.

The resultant models, shown in Figures 1(a) and 3(c) for the stowed and deployed case, respectively, served two primary objectives. Firstly, to demonstrate that the lowest NFs of the assembly would exceed 50 Hz for the launch and 10 Hz for the operational state, respectively. In principle this is challenging prior to test correlation and model updating, but the extensive overlap in topology and materials with the first-generation baffle was deemed sufficient for obtaining reliable estimates. This increased confidence in the architecture enabled streamlining the design cycles, omitting engineering model iterations altogether. Ultimately, only one qualification and one flight model (FM) were built.

Secondly, the thin-walled composite support tube introduces new mechanical failure modes dominated by elastic buckling. Initial static analyses were performed in Nastran SOL 105/400 under the following assumptions:

- Absence of initial geometric imperfections
- Approximation of the telescopic section and base plate as a rigid 6-DOF point mass
- Uniaxial inertial loading of the thrust tube

This idealised representation (Figure 3(f)) inherently renders the static predictions non-conservative. Transverse excitation of the stowed payload induces overturning moments at the interface, amplifying local compressive stresses. Furthermore, geometric imperfections and non-uniform material properties are inherent to composite manufacturing. Finally, low modal damping of structural modes with high effective mass likely induces dynamic loads generated by the telescopic substructure exceeding rigid-body approximations.

Consequently, these FEA predictions of linear eigenvalue buckling load $P_{\text{crit}}^{\text{id}}$ serve as an upper bound for the true stability limit P_{stab}. Simultaneously, a 3σ quasi-static approximation of the prescribed inputs power spectral densities (PSDs), applied to a representative equivalent rigid mass, supplies a lower bound $P_{3\sigma}$ for the maximum dynamic load $P_{\max}$ during vibration testing. Hence,

$$P_{3\sigma} \leq P_{\max}, \quad P_{\text{stab}} \leq P_{\text{crit}}^{\text{id}} \tag{1}$$

The inequalities in (1) represent a heuristic typically valid for space structures and correlated FE models thereof. Table I collates the $P_{\text{crit}}^{\text{id}}$ and $P_{3\sigma}$ values pertinent to the FM, QM and thrust tube loaded with a 4.2 kg total mass, which matches the missing full assembly components.

Table I: Idealised FEA critical buckling load and estimated 3σ test loads for a 4.2 kg rigid mass

	$P_{\text{crit}}^{\text{id}}$, N	$P_{3\sigma}$, N		
Axis	FEA	FM	QM	Tube
X	1117	954	1480	1747
Y	1104	954	1481	1747
Z	10 066	1180	1595	

B. Vibration testing

Inspecting Table I and (1), it transpires that thrust tube buckling during in-plane random vibration testing is anticipated at qualification and highly probable at acceptance levels. Thus, physical testing of the thrust tube with a conservative input before commencement of the formal campaigns was mandated. In particular, X and Y axis $P_{3\sigma}$ values correspond to 7.7, 12.0 and 14.1 g RMS profiles for the acceptance, qualification and thrust tube de-risking campaigns, respectively. The former are mission-specific, whereas the latter is the ubiquitous NASA GEVS specification.

Consequently, thrust tube in-plane vibration testing was first conducted at University of Auckland's National Satellite Test Facility (NSTF), followed respectively by the qualification and acceptance campaigns, all in the usual format

- 5–2000 Hz, 0.5 g sine sweep
- 20–2000 Hz random vibration
- 5–2000 Hz, 0.5 g sine sweep

with additional high-level sine, quasi-static loading and interim characterisation sweeps performed for the QM. Finally, 0.25 g sine sweeps in the deployed configuration were done to verify compliance with eigenfrequency requirements.

The laboratory hardware comprised a 20 kN Dongling ES-20-320 electrodynamic shaker and a Siemens SCADAS integrated data acquisition and control system. The thrust tube with dummy mass, QM and FM test articles were instrumented with 10 mV/g teardrop and triaxial ICP accelerometers as necessary. Figures 1(b) and 3 show the resultant test configurations, along with the reference coordinate system.

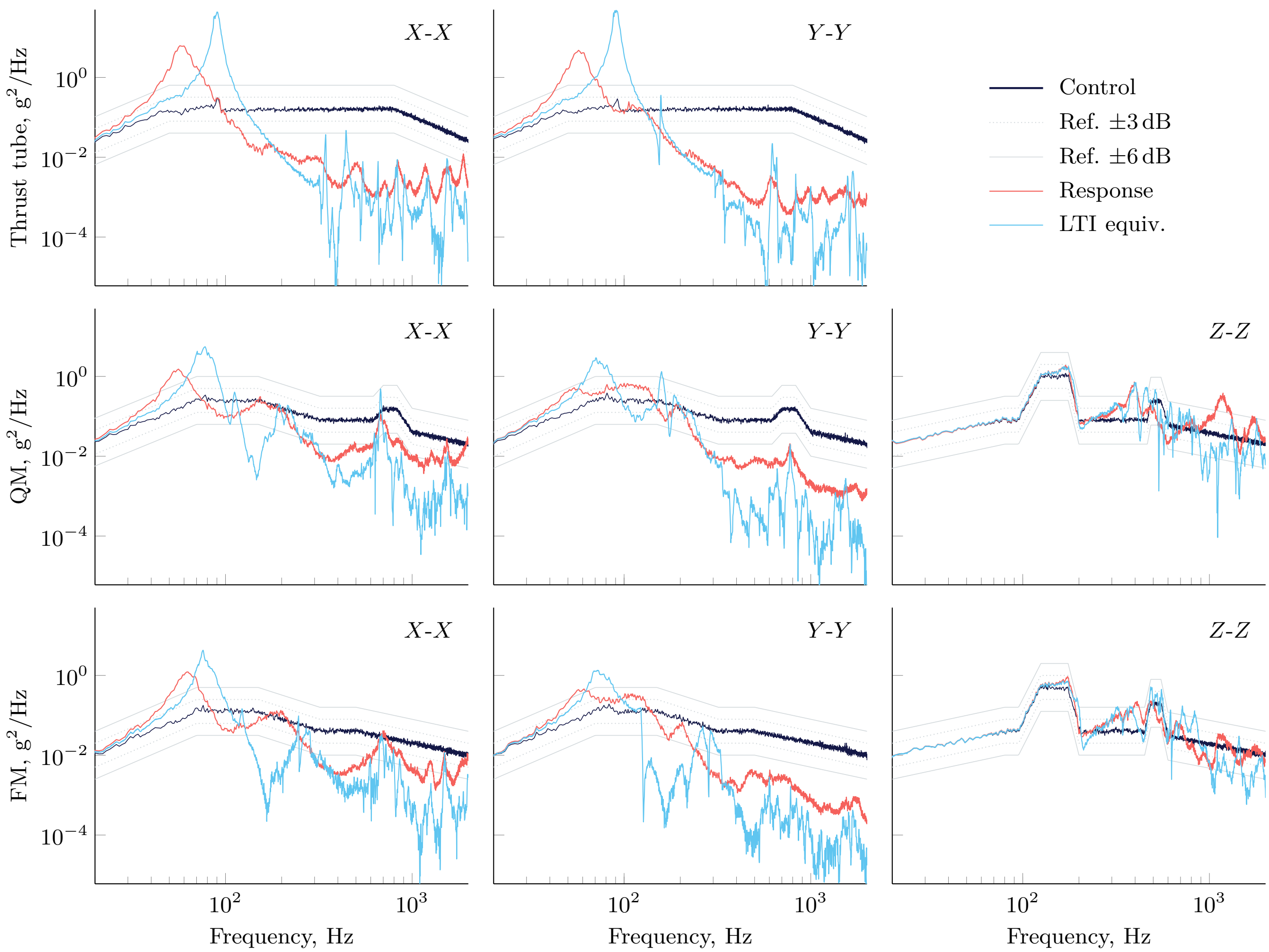

Figure 4: PSDs of the control input, measured in-axis response and synthesised LTI equivalent across all models and tests. Corresponding signal g RMS values are provided in Table II

The second-generation baffle successfully passed all tests, with first mode NFs exceeding 13 and 69 Hz in the deployed and launch configurations, respectively. No significant modal shifts, loss of fastener preload or other markers of mechanical degradation were recorded.

IV. Thrust tube nonlinear isolation

A. *Elastic snap-through*

As predicted, thrust tube intermittent buckling occurred in all lateral random vibration tests and in no axial ones. Stability limit exceedance resulted in a high-frequency snap-through, introducing a negative mean tangent stiffness contribution. As a result, dynamic reduction of the first bending eigenfrequency was observed, along with a notable increase in effective modal damping via energy scattering.

Figure 4 illustrates the in-axis responses of a sensor located on the +X side of the plate across all models, cf. Figure 1(b). The measured response PSD substantially deviates from a linear projection synthesised from the recorded control input PSD $\mathrm{X}_{\mathrm{ctrl}}(\omega)$ and the acceleration transmissibility $\mathrm{T}_{\mathrm{sweep}}(\omega)$ obtained from the post-test sine sweep, as subsequently explained in Section IV-B.

Nevertheless, the phenomenon is purely elastic, as evidenced by pre- and post-random vibration frequency response comparisons. Figure 5 shows in-axis acceleration magnitude recorded by the reference sensor. Clearly, no major shifts in eigenfrequencies or effective damping were present in sweep 2. In fact, the lowest discrepancies captured pertain to the thrust tube with dummy mass configuration, which was stressed the most by design. Hence, minor alterations in FM and QM dynamic characteristics can be attributed to the upper subassembly with a high degree of confidence.

In the context of the enforced support motions, the thrust tube's dynamic post-buckling regime operation can be viewed as mean geometric softening. Its pair of orthogonal bending modes, whose eigenfrequencies under low excitations are 69–80 Hz for the QM, FM and 88–90 Hz for the dummy mass model, exhibit geometric nonlinearity, resulting in amplitude-dependent NF shifts and spectral energy smearing.

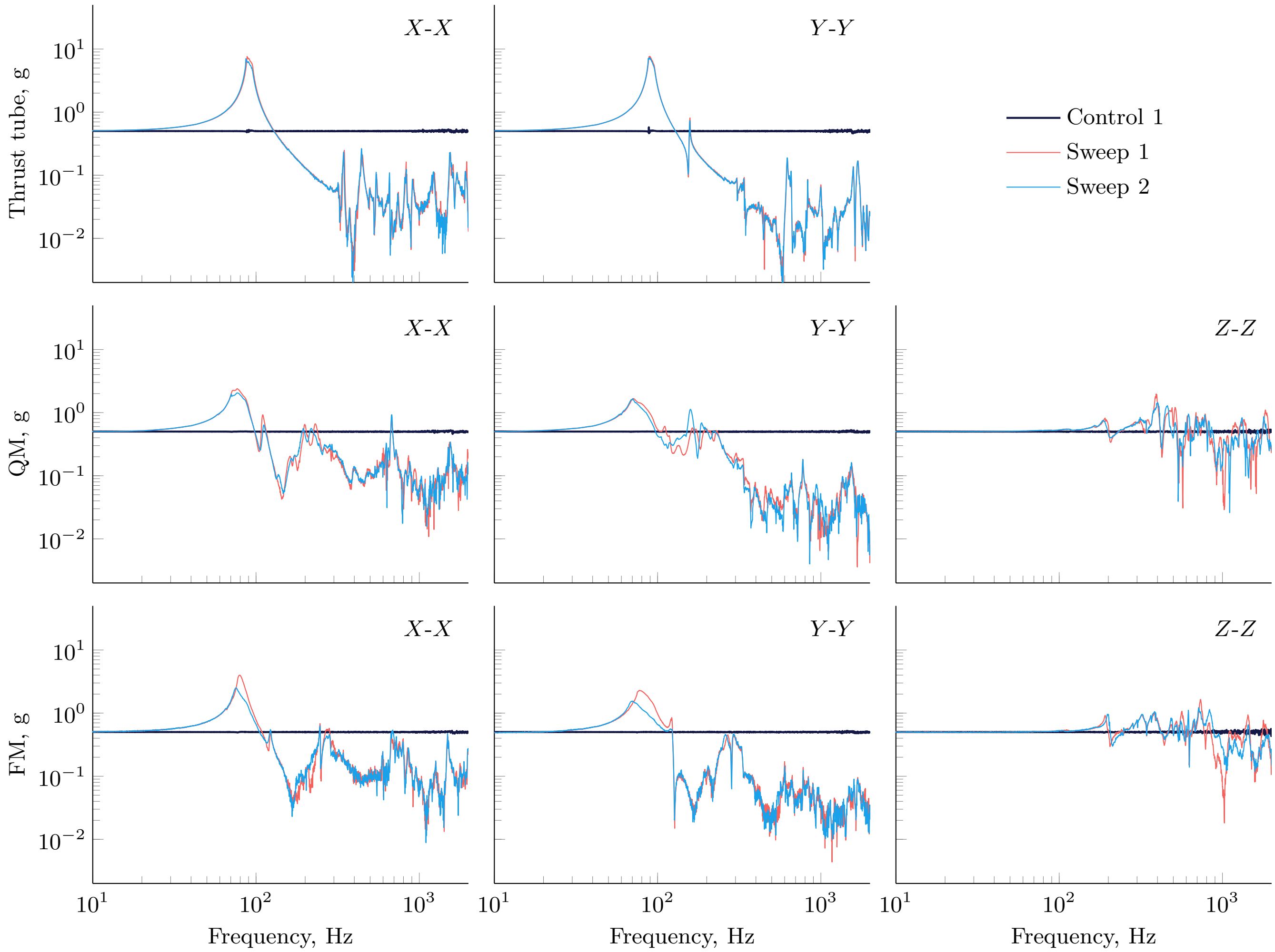

Figure 5: Comparison of in-axis response magnitudes from 0.5 g sine sweeps conducted pre- and post-random vibration. Input-output axes are indicated in the top right corner of each subplot

B. Synthesised LTI response

For a linear time-invariant (LTI) system with transfer function $\mathbf{T}_{\mathrm{RS}}(\omega)$ between output and excited DOF sets R and S, respectively, the random response $\mathbf{W}_{\mathrm{RR}}(\omega)$ is given by

$$\mathbf{W}_{\mathrm{RR}}(\omega) = \mathbf{T}_{\mathrm{RS}}(\omega)\mathbf{X}_{\mathrm{SS}}(\omega)\mathbf{T}^{*}_{\mathrm{RS}}(\omega) \tag{2}$$

Here, $\mathbf{X}_{\mathrm{SS}}$ is the input spectral density matrix and * denotes Hermitian transpose. For a 1-DOF excitation, $\mathbf{X}_{\mathrm{SS}}$ is a scalar and output PSDs become

$$\mathrm{diag}\left(\mathbf{W}_{\mathrm{RR}}(\omega)\right) = |\mathbf{T}_{\mathrm{RS}}(\omega)|^{\circ 2}\, \mathrm{X}_{\mathrm{SS}}(\omega) \tag{3}$$

where $\circ$ indicates the entry-wise square of $|\mathbf{T}_{\mathrm{RS}}|$ and diag is the diagonal extraction operator. Therefore, the LTI curve $\mathrm{W}_{\mathrm{lin}}$ in Figure 4 and linearised absolute transmissibility $|\mathrm{T}_{\mathrm{eff}}(\omega)|$ are evaluated from the available test data as

$$\mathrm{W}_{\mathrm{lin}}(\omega) = |\mathrm{T}_{\mathrm{sweep}}(\omega)|^{2}\, \mathrm{X}_{\mathrm{ctrl}}(\omega) \tag{4a}$$

$$\mathrm{W}_{\mathrm{meas}}(\omega) = |\mathrm{T}_{\mathrm{eff}}(\omega)|^{2}\, \mathrm{X}_{\mathrm{ctrl}}(\omega) \tag{4b}$$

for a single sensor channel.

Pairwise discrepancies between $\mathrm{W}_{\mathrm{lin}}$, $\mathrm{W}_{\mathrm{meas}}$ and $\mathrm{T}_{\mathrm{sweep}}$, $\mathrm{T}_{\mathrm{eff}}$ naturally induce a measure of the structure's nonlinearity between discrete load states. Under the empirically verified condition $\mathrm{T}_{\mathrm{sweep}}$ resides strictly within the linear elastic region, the metric becomes absolute with respect to it.

C. Nonlinear attenuation

Expectedly, the thrust tube's bending modes introduce a significant negative roll-off slope beyond their respective natural frequencies. Hence, attenuation of X, Y base inputs above 100–130 Hz is present irrespectively of coupling with the upper subassembly dynamics. The strength of the latter varies from negligible for the mass dummy to significant for the QM and FM baffles.

In principle, this trivial consequence of 1-DOF oscillator linear dynamics, which the baffle can be crudely approximated as with respect to the thrust tube's first bending mode, is beneficial. However, it is offset by the high amplification around the fundamental NF. This is a well-known issue characteristic of linear structural isolators.

Table II: Control input, measured response and synthesised LTI equivalent RMS accelerations, alongside relative response change Δ_{LTI} due to nonlinear attenuation

Model	Axis	Ctrl. g	Resp. g	LTI g	Δ_{LTI} %
FM	X	7.8	7.0	8.0	−12.8
	Y	7.8	5.8	6.1	−5.7
	Z	9.5	10.5	10.9	−3.4
QM	X	12.0	9.0	11.2	−20.0
	Y	12.0	8.3	9.5	−13.0
	Z	13.0	16.5	14.7	12.1
Tube	X	14.2	10.8	20.6	−47.8
	Y	14.2	9.4	21.5	−56.2

The baffle design proposed herein alleviates it by exploiting the aforesaid geometric nonlinearity. Figure 4 essentially captures time-averaged properties of the nonlinear normal modes, manifesting as softening, damping increase and energy scattering. The latter is particularly evident for the FM and QM within 120–250 Hz. The net effect is a reduced RMS transmission compared to the linear projection, as summarised in Table II, wherein Δ_{LTI} is defined as

$$\Delta_{\text{LTI}} = 100 \left(\frac{\sqrt{\int_{\omega_0}^{\omega_1} \text{W}_{\text{meas}}(\omega)\,\text{d}\omega}}{\sqrt{\int_{\omega_0}^{\omega_1} \text{W}_{\text{lin}}(\omega)\,\text{d}\omega}} - 1 \right) \tag{5}$$

In line with expectations, both the frequency of instantaneous crossings of the stability threshold P_{stab} and the mean relative time in post-buckled state increase with lateral input level. This yields, firstly, a greater negative time-averaged tangent stiffness contribution and secondly, a more prominent energy transfer pathway across frequencies via snap-through events. Mean broadband attenuation increases accordingly, as verified empirically.

Using the post-random vibration sweep for the computation in (4a) ensures that the projected linear responses in Figure 4 and Table II are conservative. The lack of measurable attenuation along Z, in spite of the greater input levels, together with the considerations from Section IV-A, confirm that the primary mechanism underpinning the RMS transmissibility loss is the geometric nonlinearity of the bending modes, as opposed to standard CFRP high-strain behaviour. Notably, the lowest NFs remained over 55 Hz across all models during high-level testing. Ultimately, two principal benefits of exploiting thrust tube post-buckling dynamics can be ascertained:

(1) Amplitude-dependent broadband attenuation compared to linear support structures
(2) Reduction in mass by avoiding unnecessary stiffening

In future work, the preliminary empirical studies conferred in this article will be extended to more datapoints such that an accurate mapping of P_{stab} and respectively the mean load-displacement properties of the thrust tube can be extracted. In turn, this would enable approximating the asymptotic limit of time-averaged transmission loss and structural survivability. It is currently uncertain to what degree the former is obfuscated by upper assembly nonlinear dynamics observed in the QM and AM tests. Subsequently, a computationally-tangible predictive model will be developed, such that a priori estimates of the expected isolation properties and elastic load limits can inform structural design.

V. Conclusions

A passive, wire-driven telescopic baffle developed for small satellite applications was introduced. It favourably combines compact stowed volume, low relative complexity and optical exclusion properties comparable to fixed rigid systems. Design and analysis activities pertaining to the second-generation architecture, featuring a fully integrated design with an opening protective lid and a composite thrust tube, were conferred.

Notably, the support tube's primary bending modes exhibit a geometric nonlinearity. Intermittent snap through under high-level lateral dynamic loads leads to softening and increased effective damping in a time-averaged sense. The effect is empirically demonstrated to be purely elastic. Broadband RMS transmission loss between the base and telescopic assembly interface of up to 56.2% in comparison to a linear response projection was recorded. Overall, exploiting the dynamic post-buckling behaviour allows simultaneous mass savings and amplitude-dependent nonlinear attenuation for the thrust tube in comparison to traditional structures.

References

[1] R. P. Heinisch and C. L. Jolliffe, "Light baffle attenuation measurements in the visible," *Applied Optics*, vol. 10, no. 9, pp. 2016–2020, 1971.

[2] C. Leinert and D. Klüppelberg, "Stray light suppression in optical space experiments," *Applied Optics*, vol. 13, no. 3, pp. 556–564, 1974.

[3] L. Wang and W. Ma, "Stray light suppression of optical and mechanical system for telescope detection," in *Proc. SPIE 8907, International Symposium on Photoelectronic Detection and Imaging 2013: Infrared Imaging and Applications*, Beijing, China, 9 2013.

[4] A. Hammar, O. M. Christensen, W. Park, S. Pak, A. Emrich, and J. Stake, "Stray light suppression of a compact off-axis telescope for a satellite-borne instrument for atmospheric research," in *Proc. SPIE 10815, Optical Design and Testing VIII, 108150F*, Beijing, China, 11 2018.

[5] L. Wei, L. Yang, Y.-P. Fan, S.-S. Cong, and Y.-S. Wang, "Research on stray-light suppression method for large off-axis three-mirror anastigmatic space camera," *Sensors*, vol. 22, no. 13, p. 4772, 2022.

[6] S.-E. Qian, *Optical payloads for space missions*. Chichester, UK: John Wiley & Sons, 2016.

[7] A. Z. Marchi, L. Maresi, and M. Taccola, "Technologies and designs for small optical missions," in *Proc. SPIE 11180, International Conference on Space Optics - ICSO 2018, 111801Z*, Chania, Greece, 7 2019.

[8] J.-J. P. Arnoux, “Star sensor baffle optimization: some helpful practical design rules,” in *Proc. SPIE 2864, Optical System Contamination V, and Stray Light and System Optimization*, Denver, CO, 11 1996.

[9] J. Haghshenas and E. Johari, “A theoretical method for vanes profile design in star sensor baffle,” in *Proc. SPIE 9264, Earth Observing Missions and Sensors: Development, Implementation, and Characterization III, 92641R*, Beijing, China, 11 2014.

[10] L. Puig, A. Barton, and N. Rando, “A review on large deployable structures for astrophysics missions,” *Acta Astronautica*, vol. 67, no. 1-2, pp. 12–26, 2010.

[11] D. Gooding, G. Richardson, A. Haslehurst, D. Smith, C. Saunders, G. S. Aglietti, R. Blows, J. Shore, K. Hampson, and M. Booth, “A novel deployable telescope to facilitate a low-cost & 1m GSD video rapid revisit small satellite constellation,” in *Proc. SPIE 11180, International Conference on Space Optics - ICSO 2018, 1118009*, Chania, Greece, 7 2019.

[12] T.-Y. Park, B.-G. Chae, and H.-U. Oh, “Development of 6U cubesat’s deployable solar panel with burn wire triggering holding and release mechanism,” *International Journal of Aerospace Engineering*, vol. 2019, 2019.

[13] J. Sauder, C. Gebara, N. H. Reddy, and C. J. García-Mora, “A framework for small satellite deployable structures and how to deploy them reliably,” *Communications Engineering*, vol. 3, p. 72, 2024.

[14] L. Dai and L. Hu, “Kinematic analysis and model fabrication of a space deployable optical baffle,” *AIAA Journal*, vol. 58, no. 3, pp. 1386–1396, 2020.

[15] J. Choi, D. Lee, K. Hwang, and B. Kim, “Design, fabrication, and evaluation of a passive deployment mechanism for deployable space telescope,” *Advances in Mechanical Engineering*, vol. 11, no. 5, p. 1687814019852258, 2019.

[16] B. Wang, J. Zhu, S. Zhong, W. Liang, and C. Guan, “Space deployable mechanics: A review of structures and smart driving,” *Materials & Design*, vol. 237, p. 112557, 2024.

[17] A. Yalagach, G. S. Aglietti, M. Honeth, S. Gensemer, and O. Diegel, “Deployable barrel for a cubesat’s optical payload,” in *AIAA SciTech Forum*, Nashville, TN, 2021, pp. 1–10.

[18] A. Yalagach, M. Honeth, R. Gandhi, G. S. Aglietti, C. Ingram, and A. Saxena, “Development of a deployable mechanism for a conical optical baffle for a small satellite,” *Advances in Space Research*, vol. 73, no. 1, pp. 870–884, 2024.

[19] M. Honeth, A. Yalagach, and G. S. Aglietti, “Wire driven mechanisms for deployable components for optical payloads,” in *Proceedings of the 36th Annual Small Satellite Conference*, Logan, UT, 2022.

[20] G. S. Aglietti, M. Honeth, M. Longato, V. Yotov, S. Hosseini, and C. Bamann, “Passive deployable baffle for space telescope,” in *18th ECSSMET*, Noordwijk, The Netherlands, 9 2024.

[21] European Cooperation for Space Standardization, *Space engineering: Testing*, ECSS, Noordwijk, The Netherlands, 2012, eCSS-E-ST-10-03C.

[22] National Aeronautics and Space Administration, *General Environmental Verification Standard (GEVS) for GSFC Flight Programs and Projects*, NASA, 2021, gSFC-STD-7000B.

[23] M. M. Bennett, “Orbital debris requires prevention and mitigation across the satellite life cycle,” *Communications Engineering*, vol. 4, p. 95, 2025.

[24] ESA Space Debris Office, *ESA Space Environment Report 2024*, European Space Agency, 2024, gEN-DB-LOG-00288-OPS-SD.

[25] I. del Portillo, B. G. Cameron, and E. F. Crawley, “A technical comparison of three low-earth-orbit satellite constellation systems to provide global broadband,” *Acta Astronautica*, vol. 159, pp. 123–135, 2019.

[26] J. C. McDowell, “The low Earth orbit satellite population and impacts of the SpaceX Starlink constellation,” *Astrophysical Journal Letters*, vol. 892, no. 2, p. L36, 2020.

[27] M. Honeth, G. S. Aglietti, M. Longato, V. Yotov, S. Hosseini, and C. Bamann, “Passively deployable telescopic baffle for enhanced LEO monitoring camera,” in *76th IAC*, Sydney, Australia, 9 2025.